Optimization of sintering conditions for improved microstructural and mechanical properties of dense $Ce_{0.8}Gd_{0.2}O_{2-\delta}$ -FeCo₂O₄ oxygen transport membranes

Fanlin Zeng^{1,2,*}, Jürgen Malzbender¹, Stefan Baumann¹, Arian Nijmeijer², Louis Winnubst², Mirko Ziegner¹, Olivier Guillon¹, Ruth Schwaiger^{1,3}, Wilhelm Albert Meulenberg^{1,2}

¹Forschungszentrum Jülich GmbH, Institute of Energy and Climate Research (IEK), 52425 Jülich, Germany ²University of Twente, Faculty of Science and Technology, Inorganic Membranes, P.O. Box 217, 7500 AE Enschede, The Netherlands

³RWTH Aachen University, Chair of Energy Engineering Materials, 52056 Aachen, Germany

Abstract

Ce_{0.8}Gd_{0.2}O_{2-δ}-FeCo₂O₄ composite is an excellent oxygen transport membrane material with good chemical stability for applications in oxygen separation and membrane reactors. To improve microstructural and mechanical properties, sintering profiles for Ce_{0.8}Gd_{0.2}O_{2-δ}-FeCo₂O₄ composites were optimized. Different sintering temperatures are selected based on our study of phase interactions among the initial powder mixtures using high-temperature X-ray diffraction. The results reveal that the phase interaction at ~1050 °C accelerates densification process, and a further increase of sintering temperature to 1200 °C contributes to the homogenization of the pore distribution. A higher density and an improved homogeneity of pore distribution result in enhanced mechanical strength. However, the density decreases once the sintering temperature reaches 1350 °C. Hence, the optimal sintering temperature considering both microstructural and mechanical properties appears to be 1200 °C. Sintering at this temperature results in a microstructure with a density exceeding 99 % with only small surface defects and a high average flexural strength of approximately ~266 MPa.

Keywords: dual-phase ceramic, oxygen transport membrane, sintering, microstructure, mechanical property, optimization

1. Introduction

Oxygen transport ceramic membrane materials have attracted great attention due to their potential economic and environmental benefits for application in oxygen separation [1-3], partial oxidation of hydrocarbons [4-6], and oxyfuel coal combustion [7-9]. Dense dual-phase ceramic composites, consisting of ionic conducting and electronic conducting phases, are deemed to be promising material candidates as oxygen transport membranes [10, 11]. They show appreciable oxygen permeability and excellent chemical stability during operation in corrosive atmospheres (e.g., SO_2 , CO_2) at elevated temperature (~850 °C) [12-21]. The 85 wt% $Ce_{0.8}Gd_{0.2}O_{2-\delta}$ - 15 wt% $FeCo_2O_4$ (CF) composite, as one typical example, maintained a stable phase structure and a constant oxygen permeation flux with the presence of flue gases at 850 °C for as long as 200 h [13]. The phase interactions between $Ce_{0.8}Gd_{0.2}O_{2-\delta}$ and $FeCo_2O_4$ appeared to be of non-hindrance to oxygen permeability since the phase interaction product, i.e., $Gd_{0.9}Ce_{0.1}Fe_{0.8}Co_{0.2}O_3$ (GCFCO) [22-24], exhibited a relatively high electrical conductivity [22,

*Corresponding author Email: f.zeng@fz-juelich.de

Tel.: ++49-2461-619399 Fax: ++49-2461-612455 23]. Similar phase interactions and phase interaction products were even reported to enhance grain boundary ionic conductivity and oxygen permeation flux of the 60 vol % $Ce_{0.8}Gd_{0.2}O_{2-\delta}$ - 40 vol% Fe_2CoO_4 composite [25].

Although the research activities on dense dual-phase oxygen transport membranes showed a preference towards chemical properties, e.g., conductivity, oxygen permeability, and chemical stability [11-21, 26-28], investigation and optimization of the mechanical properties are also indispensable for the realization of a long-term reliable operation [29-32].

Mechanical properties of most ceramic materials are governed by microstructural characteristics, e.g., defect, porosity, and grain size [33, 34]. There is a general agreement that a reduction of porosity tends to improve the mechanical properties [35-39], while the grain size effect differs for the different types of mechanical properties. For instance, hardness increases with decreasing grain size [40, 41], following a Hall-Petch relationship, while the elastic modulus usually does not depend on the grain size [39, 40, 42, 43]. A higher mechanical strength has been reported for ceramics with smaller grain size [34, 44, 45]. According to the limited reported studies [24, 30, 31, 46], the mechanical properties of dense dual-phase oxygen transport membranes show comparable dependence on microstructural characteristics such as porosity and grain size.

To improve the microstructural characteristics and the mechanical properties, optimizing the sintering profile represents an effective and straightforward way [34, 40, 47, 48]. Generally, both grain size and density of ceramic materials increase with the sintering temperature [49], which is followed by agglomeration and size-proportional growth of pores [33]. Particularly known is a de-densification phenomenon [50], i.e., the density starts to decrease with increasing sintering temperature after having reached a maximum value, as also reported for some ionic conducting ceramics [47, 51]. For example, large pores formed in zirconia sintered at temperatures above 1600 °C [47]. Similar pore formation and swelling effects were also reported for nano-size CeO₂ powder compact sintered at 1350 °C, apparently induced by oxygen gas produced by the redox reaction of Ceria [51]. Furthermore, the de-densification behavior of CeO₂ was affected by doping with Gd [48], as well as the introduction of sintering agents such as CoO [52], Bi₂O₃ [53], and Fe₂O₃ [54]. The reduced density resulting from the de-densification process was attributed to being the dominating reason for reductions of elastic modulus and mechanical strength [47, 48].

Among the studies on dual-phase oxygen transport membranes, only a few discussed the correlation between sintering profile and mechanical reliability [31, 46]. It was concluded for 50 vol% $Ce_{0.9}Gd_{0.1}O_{2-\delta}$ -50 vol% $La_{0.6}Sr_{0.4}Co_{0.2}Fe_{0.8}O_{3-\delta}$ composite that an intermediate sintering temperature of 1250 °C resulted in a relatively dense microstructure with fine grains, and thereby permitted a sufficient mechanical strength for safe application as oxygen transport membrane [46].

The current work aims for improving the microstructural and mechanical characteristics of CF composites by optimizing the sintering profiles. The abovementioned phase interactions are characterized using high-temperature X-ray diffraction. The determined phase interaction temperatures were selected as sintering temperatures to assess the effect of the phase interactions on microstructural

characteristics. The relations between the mechanical properties and the microstructural changes are discussed, and finally, an optimal sintering temperature is suggested.

2. Experimental

The composites were fabricated by solid state reaction. Powder mixtures containing 85 wt% Ce_{0.8}Gd_{0.2}O_{1.9} (Treibacher Industrie AG, 99%), 10 wt% Co₃O₄ (Alfa Aesar, 99.7%) and 5 wt% Fe₂O₃ (Sigma-Aldrich, 99%) were mixed in a plastic bottle with ethanol and zirconia balls, and ball milled on a roller bench in two steps. In the first step, the 5 mm diameter zirconia balls were used and the milling time was 3 days. In the second step, the 5 mm diameter zirconia balls were replaced with balls having 1 mm diameter, the milling time was 7 days. The ratio of powder-ball-ethanol for all the milling steps was set at 1:2:3. After drying, the powder mixtures were investigated by X-ray diffraction (see Figure S1), and Energy-dispersive X-ray spectroscopy mapping (see Figure S2). No additional phase or contamination was found. The powder mixtures were uniaxially pressed into pellets using a pressure of 19 MPa. Each pellet had a diameter of 20 mm and a thickness of ~0.8 mm. These pellets were then sintered in air at four different temperatures, i.e. 900 °C, 1050 °C, 1200 °C, and 1350 °C, respectively. The dwell time at each sintering temperature was 10 hours. The heating rate was set to 3 K/min. The cooling rate was the same, except for the temperature range between 900 °C and 800 °C, where the cooling rate was reduced to 0.5 K/min to permit a complete phase transformation from CoO rock salt to Fe_xCo_{3-x}O₄ (0 < x< 3) spinel [10]. In the following, the sintered samples are abbreviated as CF-900, CF-1050, CF-1200, and CF-1350 according to their respective sintering temperatures. For the microstructural characterization, the samples' cross-sections were ground using SiO₂-sandpaper with grit sizes ascending from 400 to 2000, and then polished using a 50 nm colloidal silica suspension including diamond paste with particle sizes stepwise reducing from 6 μ m to 3 μ m, then to 1 μ m. The last polishing stage was conducted with the 50 nm colloidal silica suspension without diamond paste. Each step was continued until the defects and scratches from the previous step were removed. Finally, the sample s' cross-sections were polished to a mirror finish.

X-ray diffraction (XRD) (Empyrean, Malvern Panalytical Ltd), equipped with a Cu long fine focus tube (40 kV / 40 mA), Bragg-Brentano^{HD} mirror (divergence = 0.4°), PIXcel3D detector (1D-mode, active length = 3.35°, 255 channels), and an Anton Paar HTK 1200N oven chamber, was used to characterize the crystal structures of the pressed powder mixtures at every 50 K during heating/cooling between room temperature and 1200 °C in air. The heating/cooling rate was 5 K/min.

Microstructures were assessed by back scattered electron microscopy (BSEM) (Merlin, Carl Zeiss Microscopy Ltd). Different phases were identified by electron backscatter diffraction (EBSD) (NordlysNano, Oxford Instruments Ltd). The grain size was then determined from image analysis using the HKL Channel 5 software packages.

The porosity was calculated as an area fraction of pores using the ImageJ software [55]. Binary pictures were generated from at least three BSEM images of polished sample cross-sections based on the isodata threshold method [56, 57]. The pores and the bulk materials in these binary pictures appeared as black and white areas, respectively.

Fracture stresses of the as-sintered pellets were assessed by ring-on-ring tests using an electromechanical testing machine (Instron 1362, Lebow Ltd) following the general procedure outlined in ASTM C1499-05 [58], but only five specimens for each composite were available for testing. The diameter and thickness of each specimen were measured with a digital micrometer with a resolution of 1 μ m. The standard deviation measured for the thickness is not larger than ~5 μ m. The specimens met the requirements for tests using loading and supporting rings with diameters of 3.43 mm and 9.99 mm, respectively. The stress rate was maintained to be 20 MPa/s. The average flexural stress (σ_f) and elastic modulus (E) were calculated by equation (1) and equation (2), respectively. The effective tensile surface areas of all samples are estimated to have similar values of ~32 mm² according to ASTM C1499-05 [58]; the Weibull modulus of Ce_{0.8}Gd_{0.2}O_{1.9} (~ 6.2 [59]) is used for the estimate.

$$\sigma_f = \frac{3F}{2\pi \cdot t^2} \cdot \left[(1 - \nu) \cdot \frac{d_s^2 - d_l^2}{2d^2} + (1 + \nu) \cdot \ln \frac{d_s}{d_l} \right] \tag{1}$$

$$E = \frac{3(1 - v^2) \cdot \left(\frac{d_l}{2}\right)^2 \cdot \Delta F}{2\pi \cdot \Delta f \cdot t^3} \cdot \left[\frac{d_s^2}{d_l^2} - 1 - \ln\frac{d_s}{d_l} + \frac{1}{2} \cdot \left(\frac{1 - v}{1 + v}\right) \cdot \left(\frac{d_s^2 - d_l^2}{d^2}\right) \cdot \frac{d_s^2}{d_l^2}\right]$$
(2)

where F is the fracture force, ΔF and Δf are the load and displacement interval of the linear part of the load-displacement curve, respectively. And d is the sample diameter, t the sample thickness, v the Poisson's ratio, d_s and d_l are the diameters of support and loading ring, respectively. Poisson's ratio was assumed to have a typical value of 0.3 [59].

The fracture surfaces were investigated through BSEM for fracture modes and fracture origins. The fracture origin size, i.e., the radius of circular/semicircular origin or minor axis length of elliptical/semielliptical origin, was measured and compared with the values estimated by equation (3) [60]:

$$\sqrt{C} = \frac{K_{IC}}{Y \cdot \sigma_f} \tag{3}$$

where C, K_{IC} , and Y are fracture origin size, fracture toughness, and stress intensity factor, respectively. Several Y values for origins with different shapes and sizes are given in ASTM C1322-15 [60].

The fracture toughness and hardness were determined using the Vickers indentation method [61], which has been effectively applied before to determine K_{IC} of the Ce_{0.9}Gd_{0.1}O_{2- δ}-La_{0.6}Sr_{0.4}Co_{0.2}Fe_{0.8}O_{3- δ} dual phase oxygen membranes [31, 44]. Vickers indentations at two different loads of 1 N and 5 N were made on the polished sample cross-sections using a macro indentation machine (Micromet® 1, Buehler Ltd). Twenty indentation tests at each load were conducted with a distance of 500 μ m between the indents. The hardness (K_{IC}) was determined by equation (4) [31]. The fracture toughness (K_{IC}) values were calculated by equation (5) with a C/α (α and α denote the measured half-diagonal of the impression and the crack length, respectively) value higher than 2.5 [61, 62].

$$H = 1.854 \cdot \frac{P}{(2a)^2} \tag{4}$$

$$K_{IC} = 0.016 \cdot \left(\frac{E}{H}\right)^{0.5} \cdot \left(\frac{P}{c}\right)^{1.5}$$
 (5)

where *P* represents the indentation load. It should be noted that equation (5) can only provide a rough estimate of the fracture toughness, which can be used for a qualitative assessment of the different samples but cannot be used for a quantitative study.

3. Results and discussion

3.1 Characterization of phase transformations

The results of the XRD in-situ observations of phase transformations within the powder compacts as a function of temperature are presented in Figure 1. Seven characteristic temperatures could be labeled with corresponding transitions listed in Table 1.

During the heating process, the Fe₂O₃ starts to form an iron cobalt spinel phase at 750 °C together with Co₃O₄. But initial diffraction patterns of the formed spinel do not fit well with that of FeCo₂O₄ spinel due to the bimodal peaks at several angles, which indicates that more than one kind of spinel, with a variation of the Fe to Co ratio, is formed. Thus, the formed spinels are denoted as Fe_xCo_{3-x}O₄ (0 < x < 3) (FCO). When the temperature increases to 900 °C, these bimodal peaks converge into unimodal peaks at the respective angles, and the spinel formed at 900 °C can be fitted well as FeCo₂O₄. At 950 °C, the FeCo₂O₄ begins to decompose into CoO and FCO. Upon further heating, the GCFCO perovskite phase appears at 1050 °C, and FCO is no longer detectable at 1150 °C. The formation of GCFCO consumes Gd from Ce_{0.8}Gd_{0.2}O_{1.9} and initiates a stoichiometry change from Ce_{0.8}Gd_{0.2}O_{1.9} to Ce_{1-y}Gd_yO_{2-δ} (0 < y < 0.2) (CGO). The GCFCO is stable once formed within the investigated temperature range, while the CoO is unstable upon cooling. The transition of CoO into FCO starts when the temperature is reduced to 900 °C, and CoO can hardly be detected anymore at 750 °C. Near the end of the experiment (100 °C - 25 °C), a small amount of Al₂O₃ materials of the oven chamber fell on the sample and produced corresponding reflections at 20 angles of 25.5°, 35.1° and 43.1°.

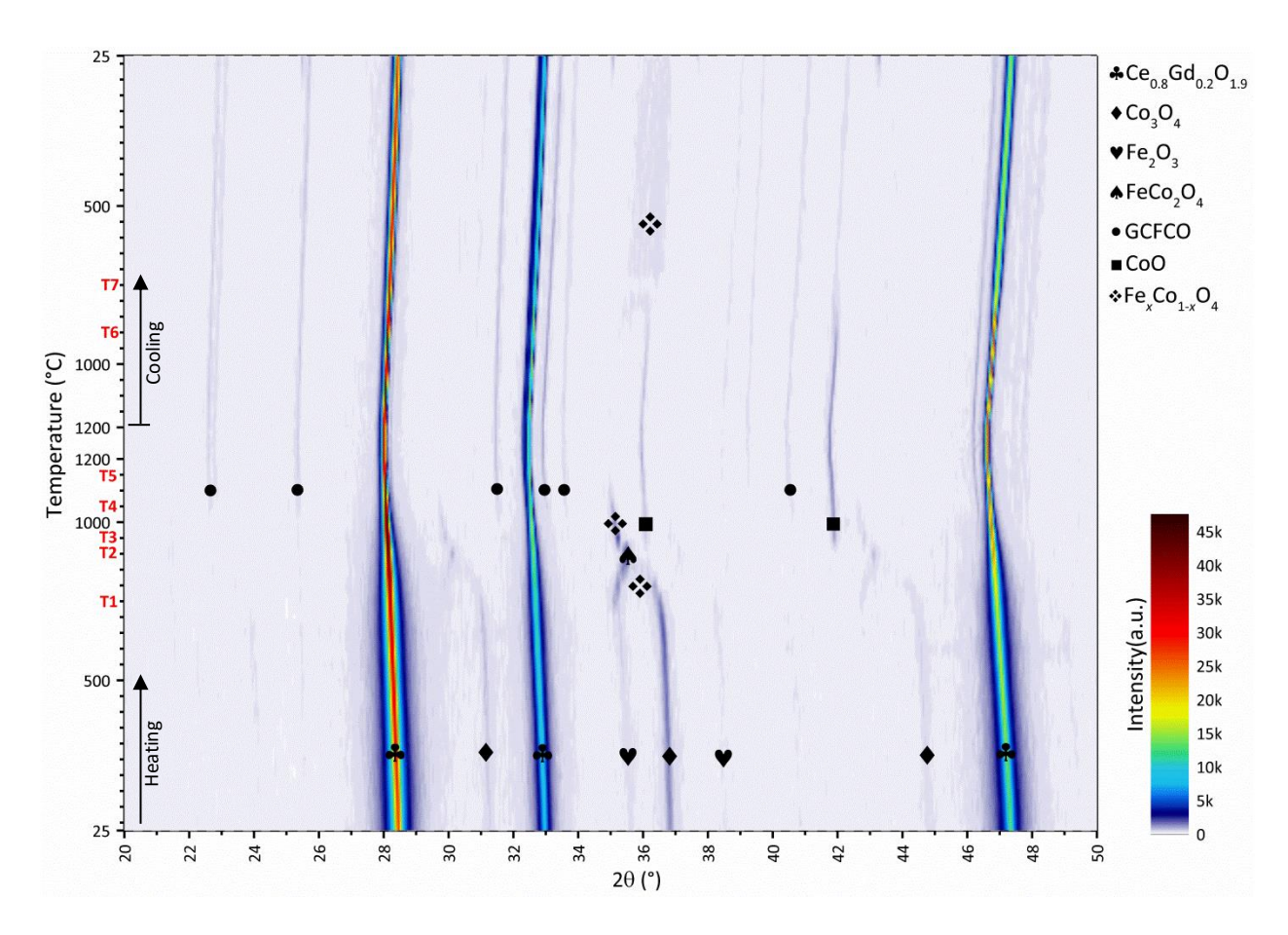


Figure 1 In-situ investigations of phase transformations of powder mixtures during heating and cooling by XRD.

Table 1 Phase transformations of powder mixtures referring to the temperatures labeled in Figure 1.

| Label | Temperature (°C) | Emerged phase | Vanished phase |
|-------|------------------|---|--|
| T1 | 750 | Fe _x Co _{3-x} O ₄ | Fe ₂ O ₃ |
| T2 | 900 | $FeCo_2O_4$ | Fe _x Co _{3-x} O ₄ |
| T3 | 950 | CoO, Fe _x Co _{3-x} O ₄ | - |
| T4 | 1050 | GCFCO, $Ce_{1-y}Gd_yO_{2-\delta}$ | - |
| T5 | 1150 | - | Fe _x Co _{3-x} O ₄ |
| Т6 | 900 | Fe _x Co _{3-x} O ₄ | - |
| T7 | 750 | - | CoO |
| | | | |

Hence, 900 °C and 1050 °C are very interesting temperatures for sintering the CF material, as phase interactions triggered at these temperatures might further influence the densification process. It should, however, be noted that these temperatures will result in CF materials with different phase constituents.

3.2 Microstructural investigations

The microstructures of samples sintered at the various temperatures are illustrated in Figure 2. Three phases can be distinguished by either intensity or topography, as indicated in Figure 2(g), for CF-1050, CF-1200, and CF-1350, whereas, only two phases are observed in CF-900, i.e., CGO and FCO, as shown in Figure 2(a)&(b). The CGO and FCO grains appear as light grey and dark grey, respectively.

The porosities of all samples were given in Table 2. Although the image-based method for porosity determination can induce large uncertainty for materials with high porosity [63], the porosity data presented here are still effective for a qualitative and in particular a relative assessment of the different samples.

CF-900 possesses the highest porosity and contains the smallest grains among all the samples, as can be seen in Table 2 and Figure 2(a)&(b), respectively. Thus, the phase interaction between the minor phases - Co_3O_4 and Fe_2O_3 at 900 °C, which results in FCO, has a limited contribution to the densification process.

By contrast, when the sintering temperature rises to $1050\,^{\circ}\text{C}$ for CF-1050, the porosity is strongly reduced to ~1.4 % (see Figure 2(c-e) and Table 2), but small pores are concentrated in a few areas as shown in Figure 2(d). This is an indication that the microstructure of CF-1050 is not homogeneously densified even though the total porosity is low. A further increase of the sintering temperature for CF-1200 helps to improve the density to ~99.3 %, and it is difficult to find areas with a significant concentration of pores (Figure 2(f,g)). Such improvement of the density for CF-1050 and CF-1200 can be attributed to the formation of the GCFCO phase. Additionally, the average grain sizes of CF-1050 and CF-1200 were characterized and analyzed on the basis of EBSD phase mapping results, see Figure S3. The grain sizes of CGO, FCO, and GCFCO in CF-1200 are ~0.5 μ m, ~0.3 μ m, and ~0.4 μ m, respectively, and around two times larger than the respective phases in CF-1050. Such a difference in grain size might affect the mechanical properties [39, 42].

Unexpectedly, when the sintering temperature is increased further to 1350 °C for CF-1350, rather large and isolated pores are formed and the total porosity increases as shown in Figure 2(h)&(i). The few pores observed in CF-1350 with sizes close to the grain size could be a result of the coarsening of the residual pores formed at lower sintering temperatures, e.g., 1200 °C. But the vast number of pores with unusually large sizes are visible in CF-1350, as shown in Figure 2(h), whereas, such large pores did not appear in CF-1200 (see Figure 2(f)). Hence, pore coarsening driven by grain growth does not appear to be the dominant mechanism for the formation of the large pores in CF-1350. Hence, the creation of oxygen gas by the reduction of Ce⁴⁺ to Ce³⁺ could be a possible origin [51]. Further investigations are necessary to clarify the mechanisms, which are out of the scope of the current work. Nevertheless, such large closed pores will induce additional oxygen exchange steps at the pore surfaces regarding oxygen permeation [64], which potentially leads to a further decrease of the permeation flux. Moreover, they might also decrease the mechanical properties [35, 65]. Hence, the sintering temperature should be limited to remain below 1350 °C.

With the goal to sinter a dense microstructure, sintering temperatures for CF material should, therefore, be between 1050 °C and 1200 °C.

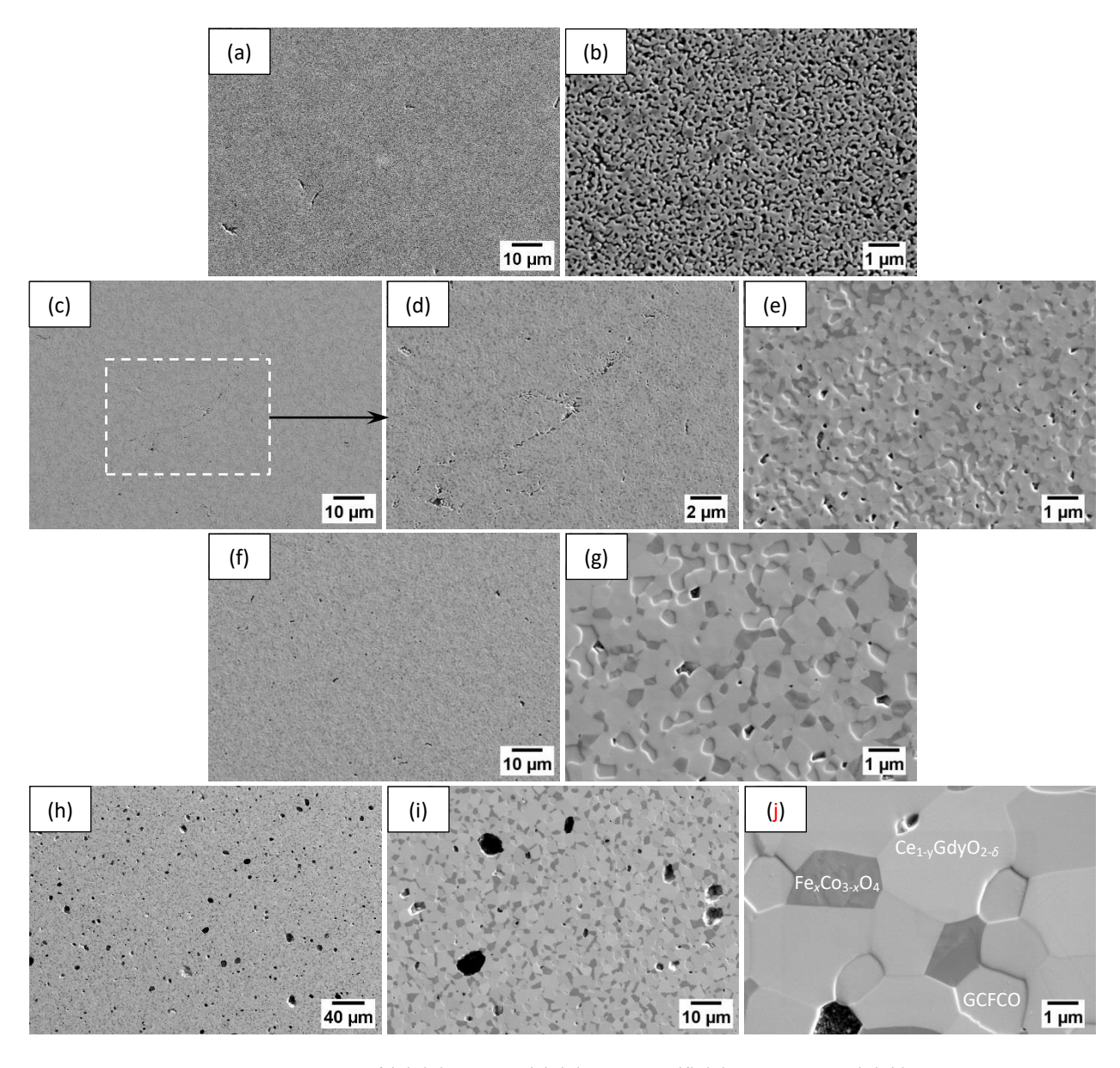


Figure 2 Microstructures of (a)-(b) CF-900, (c)-(e) CF-1050, (f)-(g) CF-1200 and (h)-(j) CF-1350.

Table 2 Porosities of the CF materials sintered at different temperatures. (± describes one standard deviation).

| Sample name | Porosity (%) | |
|-------------|----------------|--|
| CF-900 | 29.7 ± 2.2 | |
| CF-1050 | 1.4 ± 0.4 | |
| CF-1200 | 0.7 ± 0.1 | |
| CF-1350 | 2.6 ± 0.2 | |
| | | |

3.2 Mechanical properties

Since, as verified above, the first target of sintering a dense microstructure has been reached, a subsequent step is the investigation of the mechanical properties and comparison of the prepared dense samples, i.e., CF-1050 and CF-1200. It is verified by the phase and microstructure characterization results that the compositions are almost the same for CF-1050 and CF-1200. Hence, any potential difference in the mechanical properties of CF-1050 and CF-1200 should be a result of the different microstructural characteristics, i.e., porosity and grain size.

The measured mechanical properties are summarized in Table 3. The E value of CF-1200 is higher than that of CF-1050, which is mainly attributed to the higher density of CF-1200. The E value of CF-1050 exhibits a relatively high standard deviation, which is probably induced by a wide variation of porosities of the different CF-1050 samples. Such big porosity variation is not reflected in the porosity as determined from ImageJ (Table 2), though, which could be due to the fact that the image analysis represents a local measure of the porosity and that there may be more area with a greater number of pores. By contrast, the E value of CF-1200 is marginally lower than the one of CF-1050, and no load dependence is observed within the limits of the experimental uncertainty. Apparently, the porosity does not affect the hardness, while some grain boundary strengthening is observed, as explained in the following. CF-1050 possesses a finer microstructure with a larger number of grain boundaries than CF-1200, as indicated in Figure 2(e)&(g). This could be the dominant reason for the slightly higher E value of CF-1050, and any reduction of the E value of CF-1050 induced by the higher porosity is overbalanced.

Table 3 Mechanical properties of CF-1050 and CF-1200. (± describes one standard deviation).

| Sample name | E (GPa) | H (GPa) | | K_{IC} (MPa·m $^{0.5}$) | | ~ (MDa) |
|----------------|-----------|---------------|----------------|----------------------------|-----------------|------------------|
| | | 1 N | 5 N | 1 N | 5 N | σ_f (MPa) |
| CF-1050 | 163 ± 24 | 10.3 ± 0.4 | 10.0 ± 0.3 | 0.84 ± 0.04 | 0.86 ± 0.08 | 135 ± 57 |
| CF-1200 | 205 ± 5 | 9.5 ± 0.2 | 9.1 ± 0.2 | 0.86 ± 0.06 | 0.93 ± 0.07 | 266 ± 34 |

The K_{IC} values provided in Table 3 are compared to reveal potential influence from microstructural variations, but cannot be used for design purposes since the indentation method is not an ideal method for deriving accurate fracture toughness values [66]. The K_{IC} values of CF-1050 and CF-1200 are almost the same, and approximately independent of indentation loads considering the experimental uncertainties. Furthermore, the K_{IC} values are barely affected by the porosities being below ~2 %. Typical Vickers indentations after applying loads of 5 N are shown in Figure 3. Rather well-defined indentations and crack profiles can be seen. The fracture toughness of some dual-phase ceramics was reported to be influenced strongly by crack deflections [30, 67]. In addition, it was reported that cracks were attracted to the phase with the lower elastic modulus and lower thermal expansion coefficient in dual-phase ceramics [30, 31]. Since the elastic modulus and thermal expansion coefficient of the major phase constituents within the CF materials are comparable [24, 68-72], extensive crack deflections are not expected. This is confirmed by the indentation cracks that mainly pass transgranularly through the grains (see Figure S4).

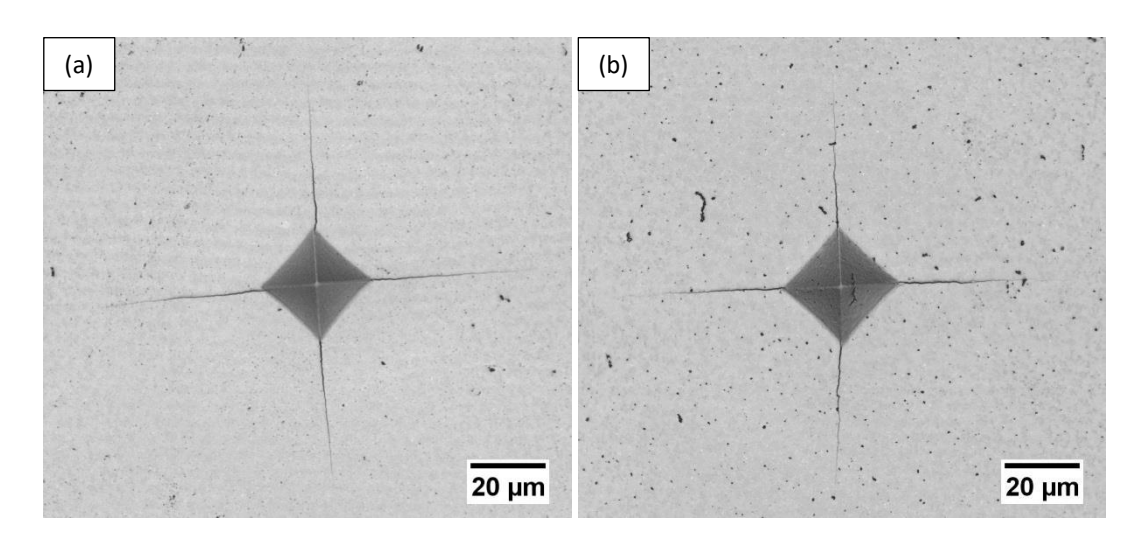


Figure 3 Vickers indentation impressions on (a) CF-1050 and (b) CF-1200 induced at a load of 5 N.

The σ_f , however, shows a large difference for CF-1050 and CF-1200 as shown in Table 3. The average σ_f of CF-1200 is almost two times higher than that of CF-1050. And it is also higher than the ones of other typical single-phase oxygen transport membranes, such as Ba_{0.5}Sr_{0.5}Co_{0.8}Fe_{0.2}O_{3- δ} (~100 MPa) [73], La_{0.58}Sr_{0.4}Co_{0.2}Fe_{0.8}O_{3- δ} (~94 MPa) [74] and SrTi_{0.65}Fe_{0.35}O_{3- δ} (~117 MPa) [75], which were tested using a similar specimen geometry.

The investigations of the fracture origins were performed on the fracture surfaces of the samples with the highest and the lowest fracture stress. The results indicate that the most likely fracture origins for CF-1050 and CF-1200 can be located near and at the tensile surface, respectively. Moreover, the measured origin size for CF-1050 is larger than that for CF-1200 (see Figure 4). Large pore agglomerations, which are similar to the pore-enriched areas as indicated in Figure 2(d), are

characterized as fracture origins in CF-1050 (see Figure 4(b)). Furthermore, the measured origin sizes are also comparable with the estimated ones considering the uncertainties induced by measurement and Y value, see Table 4.

It appears that the finer grains do not contribute to an improvement of the strength, and that the strength is governed by larger defects. However, a possible residual stress will also affect the mechanical strength, which will be the focus of our upcoming works.

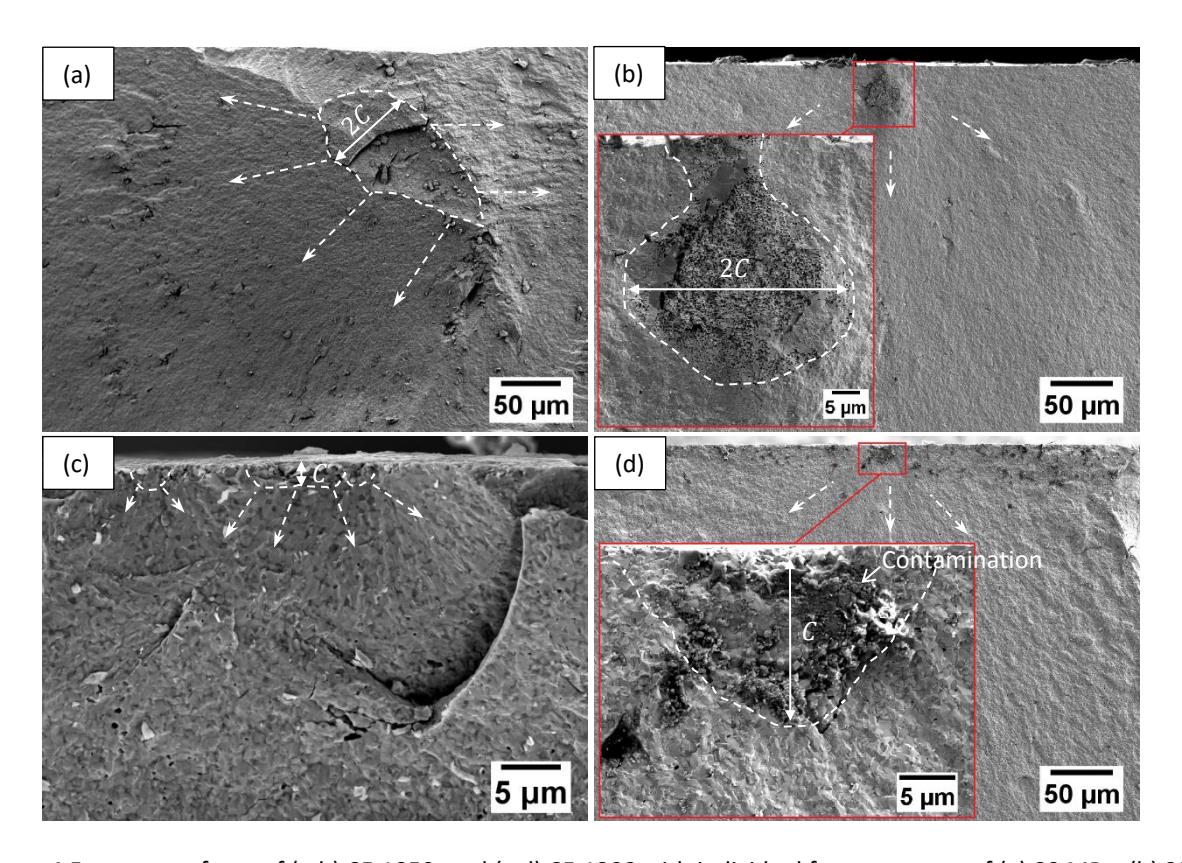


Figure 4 Fracture surfaces of (a,b) CF-1050 and (c,d) CF-1200 with individual fracture stress of (a) 80 MPa, (b) 221 MPa, (c) 212 MPa and (d) 303 MPa. The defects inside the marked regions are the possible fracture origins and the arrows are possible crack propagation paths. (Note that the dark contamination of the fracture origin in (b) did not affect the fracture stress but occurred after testing).

Table 4 Measured and estimated flaw sizes for the samples with the lowest and highest fracture stresses.

| Sample name | ரு் (MPa) | Y [60] | C (μm) – measured | C (μm) – estimated by equation 3 |
|-------------|-----------|--------|----------------------|--|
| CF 10F0 | 80 | 1.77 | 36 | 36 |
| CF-1050 | 221 | 1.13 | 19 | 12 |
| CF 4200 | 212 | 1.99 | 2 | 4 |
| CF-1200 | 303 | 1.29 | 10 | 5 |

Further observations of the fracture surfaces reveal that the fracture paths of CF-1050 and CF-1200 are mainly transgranular (Figure 5), but there are also few localized intergranular structures as can be seen in the highlighted regions in Figure 5. Our observations might indicate that the mechanical properties and the stress states of the individual phases are similar, and, therefore, the cracks do not show a clear tendency towards propagating through individual grains or along grain interfaces [29, 30]. The fracture surface of CF-1200 is more even than that of CF-1050, while large connected voids appeared in the fracture surface of CF-1050 (see the line with long dashes in Figure 5(a)). These might result from cracks propagating through regions with concentrated pores as identified in Figure 2(d).

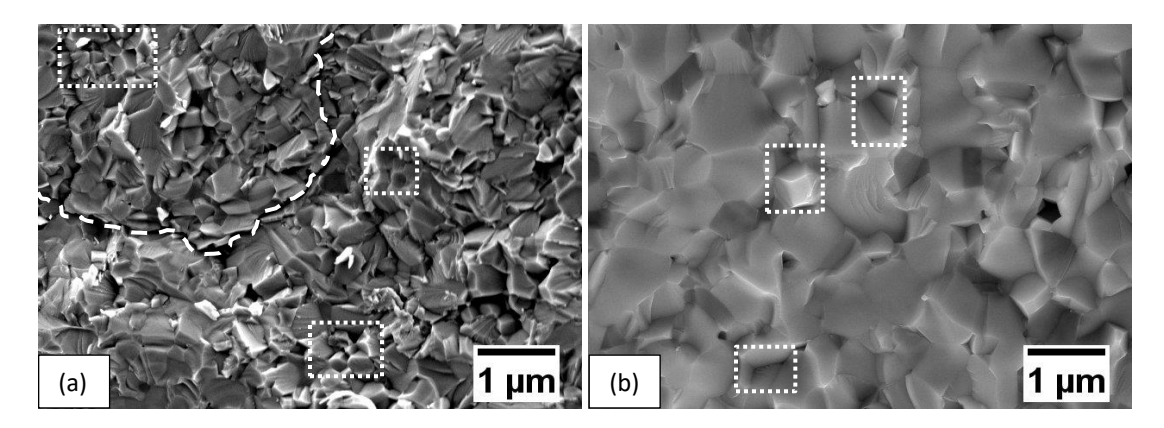


Figure 5 Fracture surfaces of (a) CF-1050 and (b) CF-1200. (The dashed line and the areas inside the marked rectangular regions denote the connected voids and some typical intergranular fracture areas, respectively)

Regarding the mechanical properties, the optimal sintering temperature for the CF material is identified as 1200 °C, since sintering at this temperature leads to a relatively high elastic modulus and high flexural strength.

4 Conclusions

CF membranes were prepared by one-step thermal processing of powder mixture of $Ce_{0.8}Gd_{0.2}O_{1.9}$, Fe_2O_3 , and Co_3O_4 . Different sintering temperatures were selected and applied according to the phase

interactions among the powder mixture characterized by high-temperature XRD. It was revealed that the formation of iron cobalt spinel and GCFCO starts at 750 °C and 1050 °C, respectively, while the formation of iron cobalt spinel has a limited contribution regarding the reduction of the porosity. The densification process is dominated by the formation of GCFCO. The membrane sintered at 1050 °C reaches an almost fully densified microstructure with rather small grains (~0.2 μ m), but a large number of small pores are concentrated in some areas. A higher sintering temperature of 1200 °C increases the density as well as the grain size, while the distribution of pores is homogenized. However, a further increase of the sintering temperature up to 1350 °C reduces the density due to the formation of large and isolated pores.

The mechanical properties of the membranes with rather dense microstructures, i.e., CF-1050 and CF-1200, are characterized and compared. The elastic modulus of CF-1050 appears to be lower than the ones of CF-1200, while the hardness of CF-1050 is slightly higher than the one of CF-1200 due to some grain boundary strengthening effects. The fracture toughnesses of CF-1050 and CF-1200 are almost identical. Besides, the flexural strength of CF-1200 is much higher than that of CF-1050. The lower strength of CF-1050 can be attributed to the larger defects that appeared in the inhomogeneously densified microstructure.

In conclusion, the optimal sintering temperature for the CF membrane, which is beneficial for both the microstructural and the mechanical properties is suggested to be 1200 °C.

Acknowledgements

This work has been funded by China Scholarship Council. The authors gratefully acknowledge Dr. E. Wessel, Dr. D. Grüner, Mr. M. Turiaux and Mr. S. Heinz for structural characterization, property testing, and sample preparation, as well as Prof. Dr. M. Krüger and Prof. Dr. L. Singheiser for support.

References

- [1] J. Sunarso, S. Baumann, J.M. Serra, W.A. Meulenberg, S. Liu, Y.S. Lin, J.C. Diniz da Costa, Mixed ionicelectronic conducting (MIEC) ceramic-based membranes for oxygen separation, Journal of Membrane Science 320(1) (2008) 13-41.
- [2] L.L. Anderson, P.A. Armstrong, R.R. Broekhuis, M.F. Carolan, J. Chen, M.D. Hutcheon, C.A. Lewinsohn, C.F. Miller, J.M. Repasky, D.M. Taylor, Advances in ion transport membrane technology for oxygen and syngas production, Solid State Ionics 288 (2016) 331-337.
- [3] P.V. Hendriksen, P.H. Larsen, M. Mogensen, F.W. Poulsen, K. Wiik, Prospects and problems of dense oxygen permeable membranes, Catalysis Today 56(1-3) (2000) 283-295.
- [4] H.J. Bouwmeester, Dense ceramic membranes for methane conversion, Catalysis Today 82(1-4) (2003) 141-150.
- [5] M.T. Ravanchi, T. Kaghazchi, A. Kargari, Application of membrane separation processes in petrochemical industry: a review, Desalination 235(1-3) (2009) 199-244.
- [6] W. Deibert, M.E. Ivanova, S. Baumann, O. Guillon, W.A. Meulenberg, Ion-conducting ceramic membrane reactors for high-temperature applications, Journal of membrane science 543 (2017) 79-97.
- [7] H. Stadler, F. Beggel, M. Habermehl, B. Persigehl, R. Kneer, M. Modigell, P. Jeschke, Oxyfuel coal combustion by efficient integration of oxygen transport membranes, International Journal of Greenhouse Gas Control 5(1) (2011) 7-15.

- [8] M. Czyperek, P. Zapp, H.J.M. Bouwmeester, M. Modigell, K. Ebert, I. Voigt, W.A. Meulenberg, L. Singheiser, D. Stöver, Gas separation membranes for zero-emission fossil power plants: MEM-BRAIN, Journal of membrane science 359(1-2) (2010) 149-159.
- [9] M. Czyperek, P. Zapp, H.J.M. Bouwmeester, M. Modigell, K.V. Peinemann, I. Voigt, W.A. Meulenberg, L. Singheiser, D. Stöver, MEM-BRAIN gas separation membranes for zero-emission fossil power plants, Energy Procedia 1(1) (2009) 303-310.
- [10] M. Ramasamy, Dual phase oxygen transport membrane for efficient oxyfuel combustion, PhD thesis, Bochum University, Bochum, Germany, 2016.
- [11] W. Fang, F. Liang, Z. Cao, F. Steinbach, A. Feldhoff, A mixed ionic and electronic conducting dual-phase membrane with high oxygen permeability, Angewandte Chemie International Edition 54(16) (2015) 4847-4850.
- [12] H. Luo, H. Jiang, K. Efimov, F. Liang, H. Wang, J.r. Caro, CO₂-tolerant oxygen-permeable Fe₂O₃-Ce_{0.9}Gd_{0.1}O_{2- δ} dual phase membranes, Industrial & Engineering Chemistry Research 50(23) (2011) 13508-13517.
- [13] M. Ramasamy, E. Persoon, S. Baumann, M. Schroeder, F. Schulze-Küppers, D. Görtz, R. Bhave, M. Bram, W. Meulenberg, Structural and chemical stability of high performance Ce_{0.8}Gd_{0.2}O_{2-δ}-FeCo₂O₄ dual phase oxygen transport membranes, Journal of Membrane Science 544 (2017) 278-286.
- [14] Z. Wang, W. Sun, Z. Zhu, T. Liu, W. Liu, A novel cobalt-free, CO₂-stable, and reduction-tolerant dual-phase oxygen-permeable membrane, ACS applied materials & interfaces 5(21) (2013) 11038-11043.
- [15] X. Zhu, Y. Liu, Y. Cong, W. Yang, $Ce_{0.85}Sm_{0.15}O_{1.925}-Sm_{0.6}Sr_{0.4}Al_{0.3}Fe_{0.7}O_3$ dual-phase membranes: one-pot synthesis and stability in a CO_2 atmosphere, Solid State Ionics 253 (2013) 57-63.
- [16] K.S. Yun, C.-Y. Yoo, S.-G. Yoon, J.H. Yu, J.H. Joo, Chemically and thermo-mechanically stable LSM-YSZ segmented oxygen permeable ceramic membrane, Journal of membrane science 486 (2015) 222-228.
- [17] H. Luo, K. Efimov, H. Jiang, A. Feldhoff, H. Wang, J. Caro, CO₂-stable and cobalt-free dual-phase membrane for oxygen separation, Angewandte Chemie International Edition 50(3) (2011) 759-763.
- [18] S. Guo, Z. Liu, J. Zhu, X. Jiang, Z. Song, W. Jin, Highly oxygen-permeable and CO_2 -stable $Ce_{0.8}Sm_{0.2}O_{2-\delta}$ -SrCo_{0.9}Nb_{0.1}O_{3- δ} dual-phase membrane for oxygen separation, Fuel Processing Technology 154 (2016) 19-26.
- [19] M. Balaguer, J. García-Fayos, C. Solís, J.M. Serra, Fast oxygen separation through SO₂- and CO₂-stable dual-phase membrane based on NiFe₂O₄-Ce_{0.8}Tb_{0.2}O_{2- δ}, Chemistry of Materials 25(24) (2013) 4986-4993.
- [20] B. Wang, J. Yi, L. Winnubst, C. Chen, Stability and oxygen permeation behavior of $Ce_{0.8}Sm_{0.2}O_{2-\delta}-La_{0.8}Sr_{0.2}CrO_{3-\delta}$ composite membrane under large oxygen partial pressure gradients, Journal of membrane science 286(1-2) (2006) 22-25.
- [21] S. Pirou, J.M. Bermudez, B.T. Na, S. Ovtar, J.H. Yu, P.V. Hendriksen, A. Kaiser, T.R. Reina, M. Millan, R. Kiebach, Performance and stability of $(ZrO_2)_{0.89}(Y_2O_3)_{0.01}(Sc_2O_3)_{0.10}$ -La $Cr_{0.85}Cu_{0.10}Ni_{0.05}O_{3-\delta}$ oxygen transport membranes under conditions relevant for oxy-fuel combustion, Journal of Membrane Science 552 (2018) 115-123.
- [22] M. Ramasamy, S. Baumann, A. Opitz, R. Iskandar, J. Mayer, D. Udomsilp, U. Breuer, M. Bram, Phase Interaction and Distribution in Mixed Ionic Electronic Conducting Ceria-Spinel Composites, Advances in Solid Oxide Fuel Cells Electronic Ceramics II: Ceramic Engineering Science Proceedings 37(3) (2017) 99-112.
- [23] F. Zeng, J. Malzbender, S. Baumann, M. Krüger, L. Winnubst, O. Guillon, W.A. Meulenberg, Phase and microstructural characterizations for Ce_{0.8}Gd_{0.2}O_{2-δ}-FeCo₂O₄ dual phase oxygen transport membranes, Journal of the European Ceramic Society, 40 (2020) 5646-5652.
- [24] F. Zeng, J. Malzbender, S. Baumann, F. Schulze-Küppers, M. Krüger, A. Nijmeijer, O. Guillon, W.A. Meulenberg, Micro-mechanical characterization of Ce_{0.8}Gd_{0.2}O_{2-δ}-FeCo₂O₄ dual phase oxygen transport membranes, Advanced Engineering Materials (2020) 1901558.

- [25] Y. Lin, S. Fang, D. Su, K.S. Brinkman, F. Chen, Enhancing grain boundary ionic conductivity in mixed ionic-electronic conductors, Nature communications 6 (2015) 6824.
- [26] Y. He, L. Shi, F. Wu, W. Xie, S. Wang, D. Yan, P. Liu, M.-R. Li, J. Caro, H. Luo, A novel dual phase membrane 40 wt% $Nd_{0.6}Sr_{0.4}CoO_{3-\delta}$ -60 wt% $Ce_{0.9}Nd_{0.1}O_{2-\delta}$: design, synthesis and properties, Journal of Materials Chemistry A 6(1) (2018) 84-92.
- [27] Y. Ji, J.A. Kilner, M.F. Carolan, Electrical conductivity and oxygen transfer in gadolinia-doped ceria (CGO)-Co₃O_{4- δ} composites, Journal of the European Ceramic Society 24(14) (2004) 3613-3616.
- [28] V.V. Kharton, A.V. Kovalevsky, A.P. Viskup, F.M. Figueiredo, A.A. Yaremchenko, E.N. Naumovich, F.M.B. Marques, Oxygen Permeability of $Ce_{0.8}Gd_{0.2}O_{2-\delta}-La_{0.7}Sr_{0.3}MnO_{3-\delta}$ Composite Membranes, Journal of the Electrochemical Society 147(7) (2000) 2814-2821.
- [29] P.-M. Geffroy, J. Fouletier, N. Richet, T. Chartier, Rational selection of MIEC materials in energy production processes, Chemical engineering science 87 (2013) 408-433.
- [30] T. Nithyanantham, S. Biswas, N. Nagendra, S. Bandopadhyay, Studies on mechanical behavior of LSFT-CGO dual-phase membranes at elevated temperatures in ambient air and slightly reducing environments, Ceramics International 40(6) (2014) 7783-7790.
- [31] S. Kim, S.H. Kim, K.S. Lee, J.H. Yu, Y.-H. Seong, I.S. Han, Mechanical properties of LSCF ($La_{0.6}Sr_{0.4}Co_{0.2}Fe_{0.8}O_{3-\delta}$)-GDC ($Ce_{0.9}Gd_{0.1}O_{2-\delta}$) for oxygen transport membranes, Ceramics International 43(2) (2017) 1916-1921.
- [32] S. Lia, W. Jin, N. Xu, J. Shi, Mechanical strength, and oxygen and electronic transport properties of $SrCo_{0.4}Fe_{0.6}O_{3-\delta}$ -YSZ membranes, Journal of Membrane Science 186(2) (2001) 195-204.
- [33] J.L. Shi, Relation between coarsening and densification in solid-state sintering of ceramics: Experimental test on superfine zirconia powder compacts, Journal of materials research 14(4) (1999) 1389-1397.
- [34] J.B. Wachtman, W.R. Cannon, M.J. Matthewson, Mechanical properties of ceramics, Wiley, Hoboken, USA, 2009.
- [35] R. Pal, Porosity-dependence of effective mechanical properties of pore-solid composite materials, Journal of Composite Materials 39(13) (2005) 1147-1158.
- [36] M. Lipińska-Chwałek, F. Schulze-Küppers, J. Malzbender, Mechanical properties of pure and doped cerium oxide, Journal of the European Ceramic Society 35(5) (2015) 1539-1547.
- [37] R.M. Spriggs, Effect of Open and Closed Pores on Elastic Moduli of Polycrystalline Ahmina, Journal of the American Ceramic Society 45(9) (1962) 454-454.
- [38] R.W. Rice, Microstructure dependence of mechanical behavior of ceramics, Treatise on Materials Science & Technology 11 (1977) 199-381.
- [39] R. Chaim, M. Hefetz, Effect of grain size on elastic modulus and hardness of nanocrystalline ZrO_2 -3 wt% Y_2O_3 ceramic, Journal of materials science 39(9) (2004) 3057-3061.
- [40] M. Yan, T. Mori, J. Zou, H. Huang, J. Drennan, Microstructures and mechanical properties of $Ce_{1-x}Ca_xO_{2-y}$ (x = 0.05, 0.1, 0.2) with different sintering temperatures, Journal of the European Ceramic Society 30(3) (2010) 669-675.
- [41] M. Trunec, Effect of grain size on mechanical properties of 3Y-TZP ceramics, Ceramics–Silikáty 52 (2008) 165-71.
- [42] O. Tokariev, L. Schnetter, T. Beck, J. Malzbender, Grain size effect on the mechanical properties of transparent spinel ceramics, Journal of the European Ceramic Society 33(4) (2013) 749-757.
- [43] J. Zhou, Y. Li, R. Zhu, Z. Zhang, The grain size and porosity dependent elastic moduli and yield strength of nanocrystalline ceramics, Materials Science and Engineering: A 445 (2007) 717-724.
- [44] E. Orowan, Fracture and strength of solids, Reports on progress in physics 12(1) (1949) 185.
- [45] A. Zimmermann, J. Rödel, Generalized Orowan-Petch plot for brittle fracture, Journal of the American Ceramic Society 81(10) (1998) 2527-2532.

- [46] K. Raju, S. Kim, C.J. Hyung, J.H. Yu, Y.-H. Seong, S.-H. Kim, I.-S. Han, Optimal sintering temperature for $Ce_{0.9}Gd_{0.1}O_{2-\delta}$ - $La_{0.6}Sr_{0.4}Co_{0.2}Fe_{0.8}O_{3-\delta}$ composites evaluated through their microstructural, mechanical and elastic properties, Ceramics International 45(1) (2019) 1460-1463.
- [47] B. Stawarczyk, M. Özcan, L. Hallmann, A. Ender, A. Mehl, C.H.F. Hämmerlet, The effect of zirconia sintering temperature on flexural strength, grain size, and contrast ratio, Clinical oral investigations 17(1) (2013) 269-274.
- [48] K. Yasuda, K. Uemura, T. Shiota, Sintering and mechanical properties of gadolinium-doped ceria ceramics, Journal of Physics: Conference Series 339 (2012) 012006.
- [49] M.N. Rahaman, Sintering of ceramics, CRC press, University of Missouri-Rolla, USA, 2007.
- [50] C. Chambon, S. Vaudez, J.M. Heintz, De-densification mechanisms of yttria-doped cerium oxide during sintering in a reducing atmosphere, Journal of the American Ceramic Society 101(11) (2018) 4956-4967.
- [51] Y. Zhou, M.N. Rahaman, Effect of redox reaction on the sintering behavior of cerium oxide, Acta materialia 45(9) (1997) 3635-3639.
- [52] T. Zhang, P. Hing, H. Huang, J. Kilner, Sintering and grain growth of CoO-doped CeO₂ ceramics, Journal of the European Ceramic Society 22(1) (2002) 27-34.
- [53] V. Gil, J. Tartaj, C. Moure, P. Durán, Sintering, microstructural development, and electrical properties of gadolinia-doped ceria electrolyte with bismuth oxide as a sintering aid, Journal of the European Ceramic Society 26(15) (2006) 3161-3171.
- [54] T. Zhang, P. Hing, H. Huang, J. Kilner, Densification, microstructure and grain growth in the CeO₂-Fe₂O₃ system ($0 \le \text{Fe/Ce} \le 20\%$), Journal of the European Ceramic Society 21(12) (2001) 2221-2228.
- [55] C.A. Schneider, W.S. Rasband, K.W. Eliceiri, NIH Image to ImageJ: 25 years of image analysis, Nature methods 9(7) (2012) 671-675.
- [56] S.M. Hartig, Basic Image Analysis and Manipulation in ImageJ, Current Protocols in Molecular Biology 102(1) (2013) 14-15.
- [57] T.W. Ridler, S. Calvard, Picture Thresholding Using an Iterative Selection Method, Ieee T Syst Man Cyb 8(8) (1978) 630-632.
- [58] ASTM, C1499-05: Standard test method for monotonic equibiaxial flexural strength of advanced ceramics at ambient temperature, ASTM International, West Conshohocken, PA, 2003.
- [59] A. Atkinson, A. Selcuk, Mechanical behaviour of ceramic oxygen ion-conducting membranes, Solid State Ionics 134(1-2) (2000) 59-66.
- [60] ASTM, C1322-15: Standard practice for fractography and characterization of fracture origins in advanced ceramics, ASTM International, West Conshohocken, PA, 2010.
- [61] G.R. Anstis, P. Chantikul, B.R. Lawn, D.B. Marshall, A critical evaluation of indentation techniques for measuring fracture toughness: I, direct crack measurements, Journal of the American Ceramic Society 64(9) (1981) 533-538.
- [62] K. Niihara, R. Morena, D.P.H. Hasselman, Evaluation of K_{IC} of brittle solids by the indentation method with low crack-to-indent ratios, Journal of materials science letters 1(1) (1982) 13-16.
- [63] M.R. Hossen, M.W. Talbot, R. Kennard, D.W. Bousfield, M.D. Mason, A comparative study of methods for porosity determination of cellulose based porous materials, Cellulose 27(12) (2020) 6849-6860.
- [64] Z. Wang, H. Liu, X. Tan, Y. Jin, S. Liu, Improvement of the oxygen permeation through perovskite hollow fibre membranes by surface acid-modification, Journal of Membrane Science 345(1-2) (2009) 65-73.
- [65] G. Pećanac, S. Foghmoes, M. Lipińska-Chwałek, S. Baumann, T. Beck, J. Malzbender, Strength degradation and failure limits of dense and porous ceramic membrane materials, Journal of the European Ceramic Society 33(13-14) (2013) 2689-2698.

- [66] G.D. Quinn, R.C. Bradt, On the Vickers Indentation Fracture Toughness Test, Journal of the American Ceramic Society 90(3) (2007) 673-680.
- [67] P. Bhargava, B.R. Patterson, Quantitative Characterization of Indentation Crack Path in a Cubic Zirconia-10 vol% Alumina Composite, Journal of the American Ceramic Society 80(7) (1997) 1863-1867. [68] K. Orlinski, R. Diduszko, M. Kopcewicz, D.A. Pawlak, The influence of chromium substitution on crystal structure and shift of Néel transition in GdFe_{1-x}Cr_xO₃ mixed oxides, Journal of Thermal Analysis Calorimetry 127(1) (2017) 181-187.
- [69] R. Korobko, C.T. Chen, S. Kim, S.R. Cohen, E. Wachtel, N. Yavo, I. Lubomirsky, Influence of Gd content on the room temperature mechanical properties of Gd-doped ceria, Scripta Mater 66(3-4) (2012) 155-158.
- [70] Z. Zhang, J. Koppensteiner, W. Schranz, M.A. Carpenter, Variations in elastic and anelastic properties of Co₃O₄ due to magnetic and spin-state transitions, American Mineralogist 97(2-3) (2012) 399-406.
- [71] A.S. Verma, A. Kumar, Bulk modulus of cubic perovskites, Journal of Alloys and Compounds 541 (2012) 210-214.
- [72] M. Ramasamy, S. Baumann, J. Palisaitis, F. Schulze-Küppers, M. Balaguer, D. Kim, W.A. Meulenberg, J. Mayer, R. Bhave, O. Guillon, Influence of Microstructure and Surface Activation of Dual-Phase Membrane Ce_{0.8}Gd_{0.2}O_{2-δ}-FeCo₂O₄ on Oxygen Permeation, Journal of the American Ceramic Society 99(1) (2016) 349-355.
- [73] B.X. Huang, J. Malzbender, R.W. Steinbrech, L. Singheiser, Discussion of the complex thermomechanical behavior of Ba_{0.5}Sr_{0.5}Co_{0.8}Fe_{0.2}O_{3-δ}, Journal of Membrane Science 359(1) (2010) 80-85. [74] B. Huang, J. Malzbender, R. Steinbrech, E. Wessel, H. Penkalla, L. Singheiser, Mechanical aspects of ferro-elastic behavior and phase composition of La_{0.58}Sr_{0.4}Co_{0.2}Fe_{0.8}O_{3-δ}, Journal of Membrane Science 349(1-2) (2010) 183-188.
- [75] R.O. Silva, J. Malzbender, F. Schulze-Küppers, S. Baumann, O. Guillon, Mechanical properties and lifetime predictions of dense $SrTi_{1-x}Fe_xO_{3-\delta}$ (x = 0.25, 0.35, 0.5), Journal of the European Ceramic Society 37(7) (2017) 2629-2636.